Plasma 2
Lecture 7: Kinetic Description of Magnetized Plasma Waves

APPH E6102y
Columbia University

10

Waves in a Hot Magnetized Plasma

$$\mathbf{v} \times \mathbf{B}_0 \cdot \boldsymbol{\nabla}_{\mathbf{v}} f_{s0} = 0 \tag{10.1.2}$$

$$\frac{\partial f_s}{\partial t} + \mathbf{v} \cdot \boldsymbol{\nabla} f_s + \frac{e_s}{m_s}(\mathbf{v} \times \mathbf{B}_0) \cdot \boldsymbol{\nabla}_{\mathbf{v}} f_s + \frac{e_s}{m_s}[\mathbf{E} + \mathbf{v} \times \mathbf{B}] \cdot \boldsymbol{\nabla}_{\mathbf{v}} f_{s0} = 0, \tag{10.1.3}$$

Plasma Physics, Vol. 16, pp. 499 to 507. Pergamon Press 1974. Printed in Northern Ireland

ELECTRON TEMPERATURE MEASUREMENTS IN A DENSE PLASMA USING BERNSTEIN WAVES

C. CHRISTOPOULOS and P. J. CHRISTIANSEN
Plasma Physics Group,
School of Mathematical and Physical Sciences,
University of Sussex, Brighton, BN1 9QH, Sussex, U.K.

(*Received* 29 *March* 1973; *and in final form* 20 *September* 1973)

Abstract—Bernstein (electron cyclotron) waves have been successfully excited and detected in a fairly dense r.f. Argon plasma. The use of these waves as a diagnostic tool in studying the thermal properties of the plasma in the direction perpendicular to an applied magnetic field has been investigated. The method could be useful in probing a wide variety of laboratory plasmas.

cussed later. Thus at high values of ω_p/ω_c the electron temperature is inferred from essentially a single parameter fit ($V_\perp$), giving $T_{e_\perp} = 2{\cdot}75$ eV.

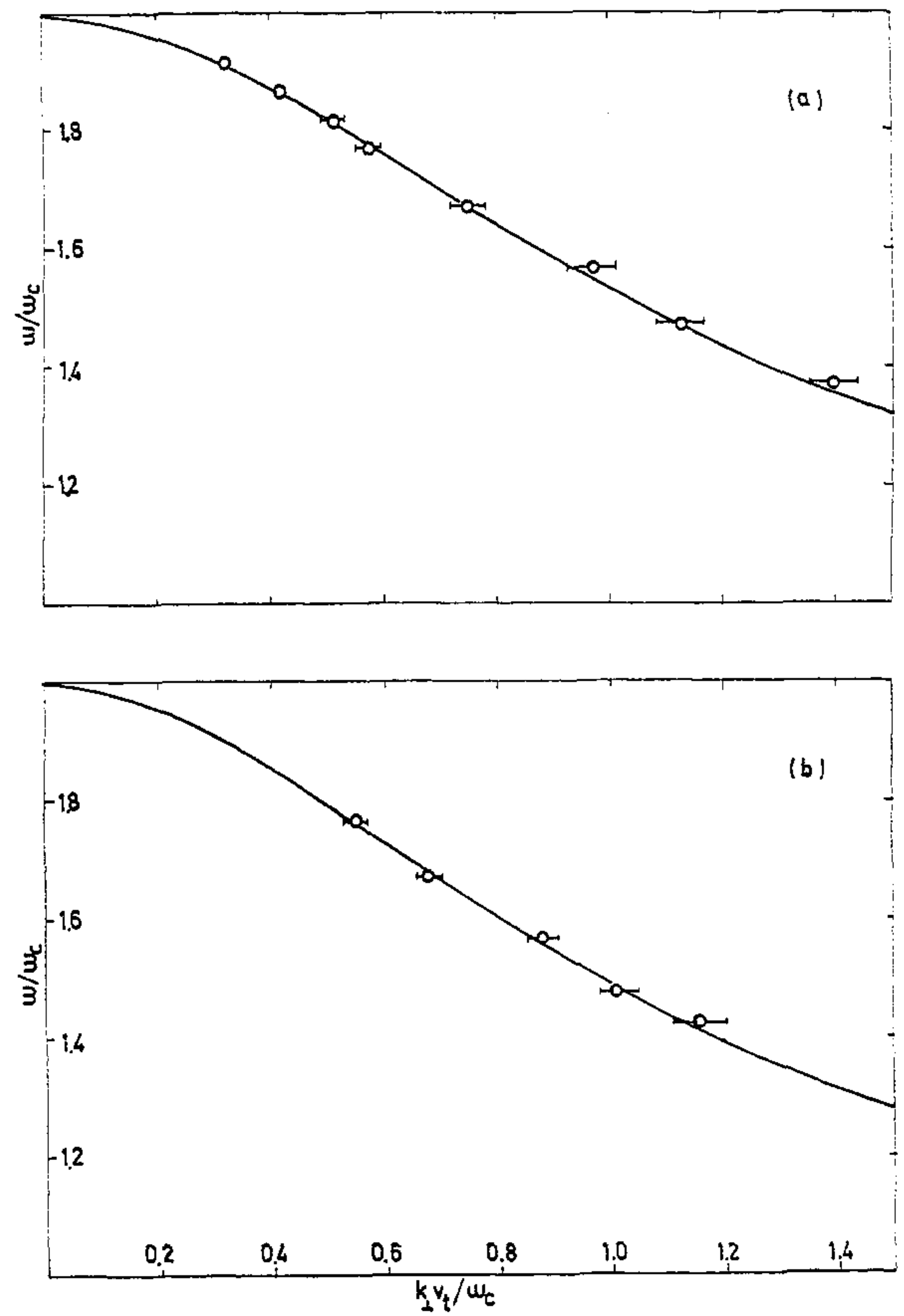

FIG. 6.—Comparison of theoretical dispersion curves and experimental data for $B_0 = 357$ G and pressure = 1m torr.
(a) $\omega_p/\omega_c = 5$ $V_\perp = 0{\cdot}98 \,.\, 10^8$ cm/sec
(b) $\omega_p/\omega_c = 3{\cdot}25$ $V_\perp = 0{\cdot}98 \,.\, 10^8$ cm/sec.

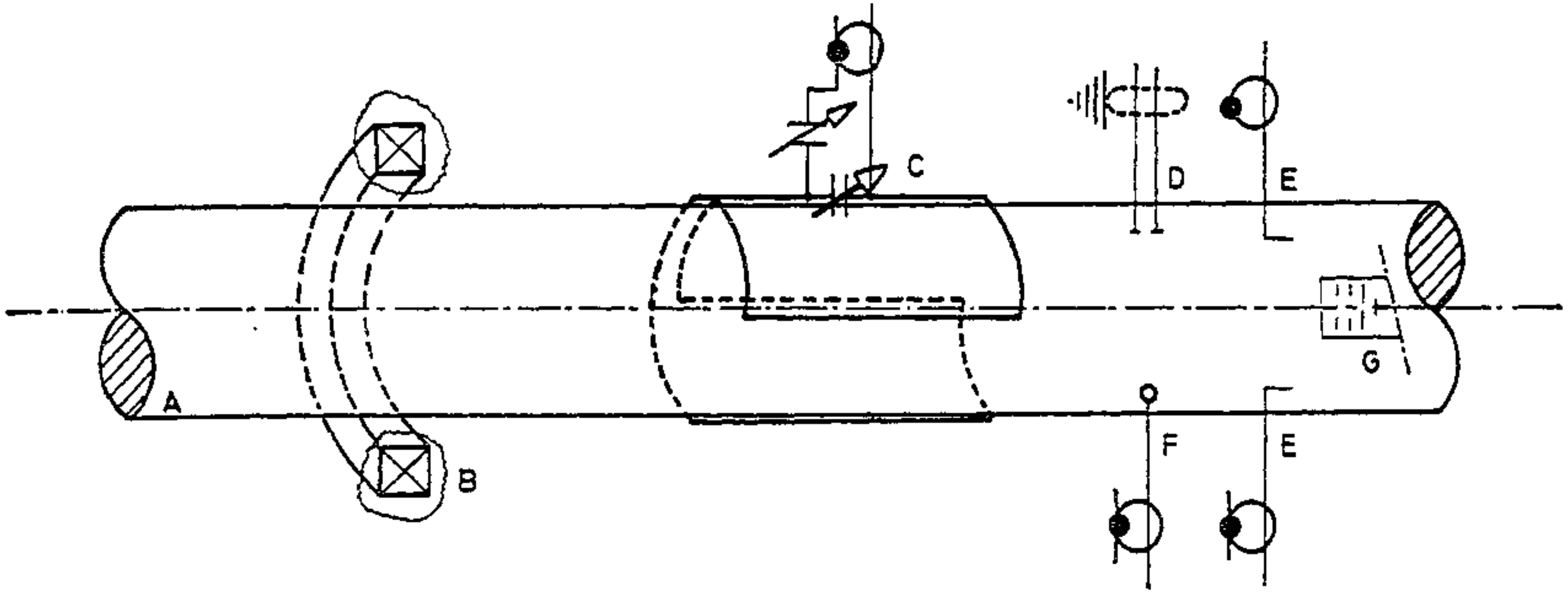

FIG. 1.—Schematic diagram of experimental apparatus: A: pyrex tube, B: axial magnetic field coil (one of 17), C: r.f. coil and matching circuit, D: double Langmuir probe, E: *L*-shaped aerials, F: magnetic probe, G: Electrostatic energy analyser.

3.1 *Experimental apparatus*

The plasma was produced by a 1·2 m long 10 cm in dia. pyrex tube immersed in an axial uniform magnetic field variable between zero and 700 G. r.f. Power from a 8·5 MHz 0·5 kW oscillator was matched into a coil surrounding the plasma and having its axis perpendicular to the axis of the discharge tube Fig. 1. The r.f. power couples into an $m = 1$ standing helicon wave (BOSWELL, 1970) as indicated by measurements of the b_θ component of the wave field inside the tube. The frequency and wavelength of the helicon waves are determined by the exciting frequency and the dimensions of the exciting coil respectively.

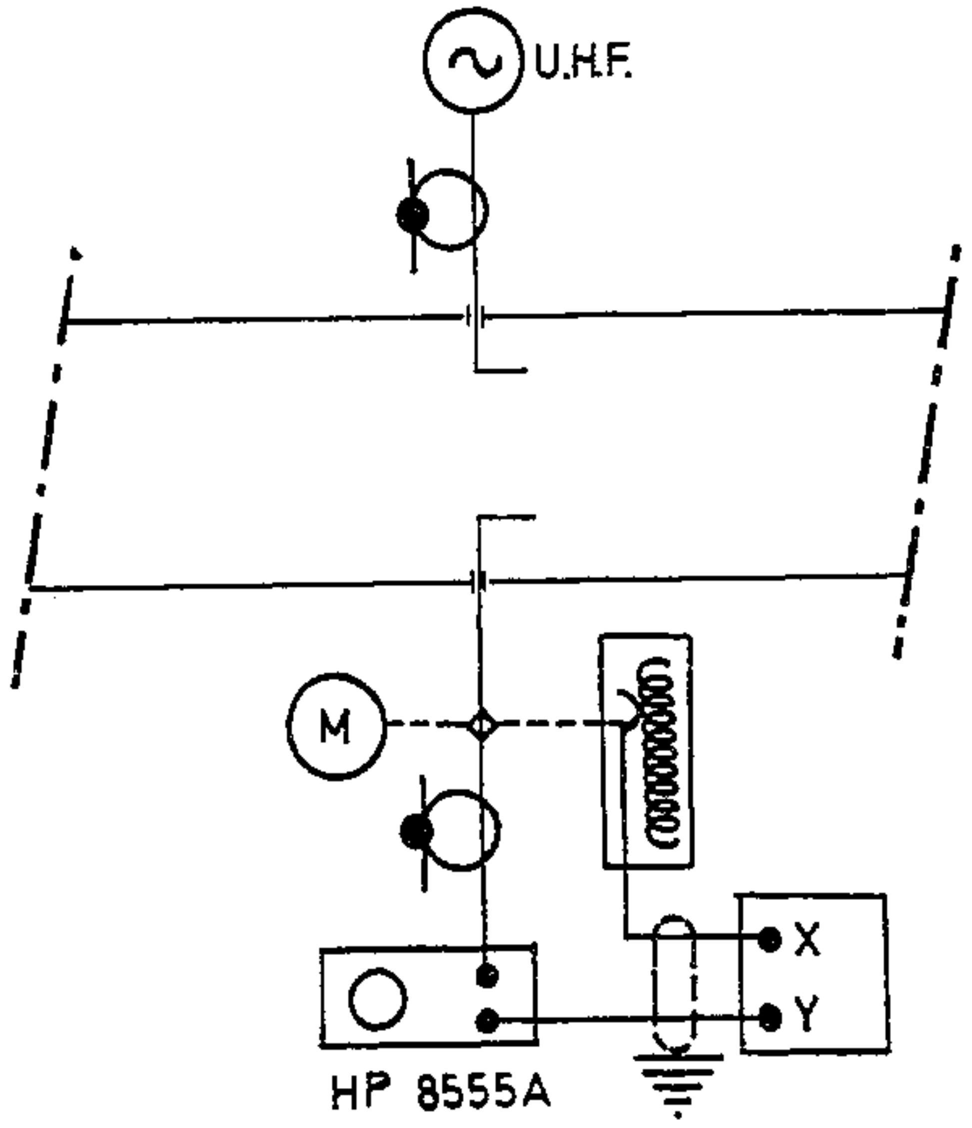

FIG. 4.—Set-up for Bernstein wavelength measurements, showing u.h.f. generator connected to fixed aerial, movable aerial and motor drive, and method of display using spectrum analyser and X–Y plotter.

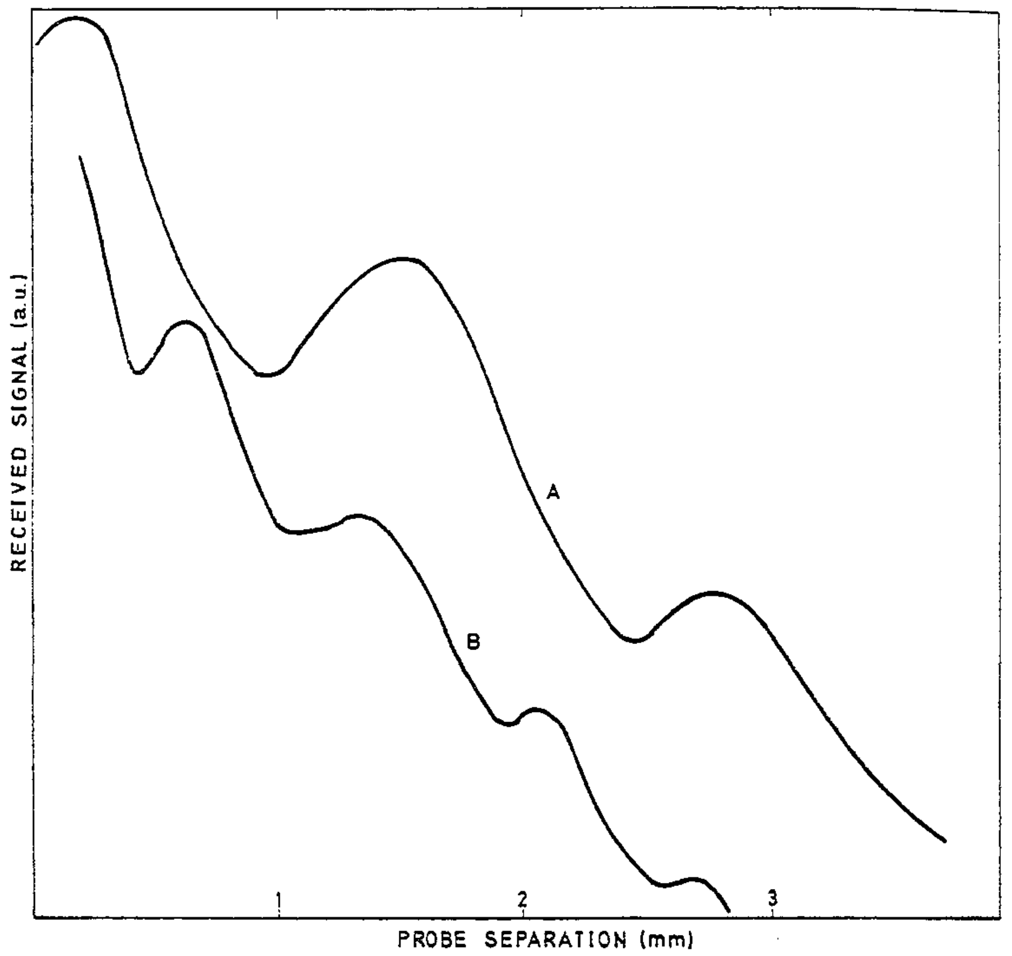

FIG. 5.—Typical received signals using arrangement of Fig. 4. Electron cyclotron frequency $f_c = 1130$ MHz, Curve *A* for $f = 2000$ MHz, Curve *B* for $f = 1650$ MHz.

JOURNAL OF GEOPHYSICAL RESEARCH, VOL. 98, NO. A12, PAGES 21,163–21,176, DECEMBER 1, 1993

Bernstein Waves in the Io Plasma Torus: A Novel Kind of Electron Temperature Sensor

NICOLE MEYER-VERNET, SANG HOANG, AND MICHEL MONCUQUET

Département de Recherche Spatiale, Centre National de la Recherche Scientifique, Observatoire de Paris, France

During Ulysses passage through the Io plasma torus, along a basically north-to-south trajectory crossing the magnetic equator at $R \sim 7.8\ R_J$ from Jupiter, the Unified Radio and Plasma Wave experiment observed weakly banded emissions with well-defined minima at gyroharmonics. These noise bands are interpreted as stable electrostatic fluctuations in Bernstein modes. The finite size of the antenna is shown to produce an apparent polarization depending on the wavelength, so that measuring the spin modulation as a function of frequency yields the gyroradius and thus the local cold electron temperature. This determination is not affected by a very small concentration of suprathermal electrons, is independent of any gain calibration, and does not require an independent magnetic field measurement. We find that the temperature increases with latitude, from $\sim 1.3 \times 10^5$ K near the magnetic (or centrifugal) equator, to approximately twice this value at $\pm 10°$ latitude (i.e., a distance of $\sim 1.3\ R_J$ from the magnetic equatorial plane). As a by-product, we also deduce the magnetic field strength with a few percent error.

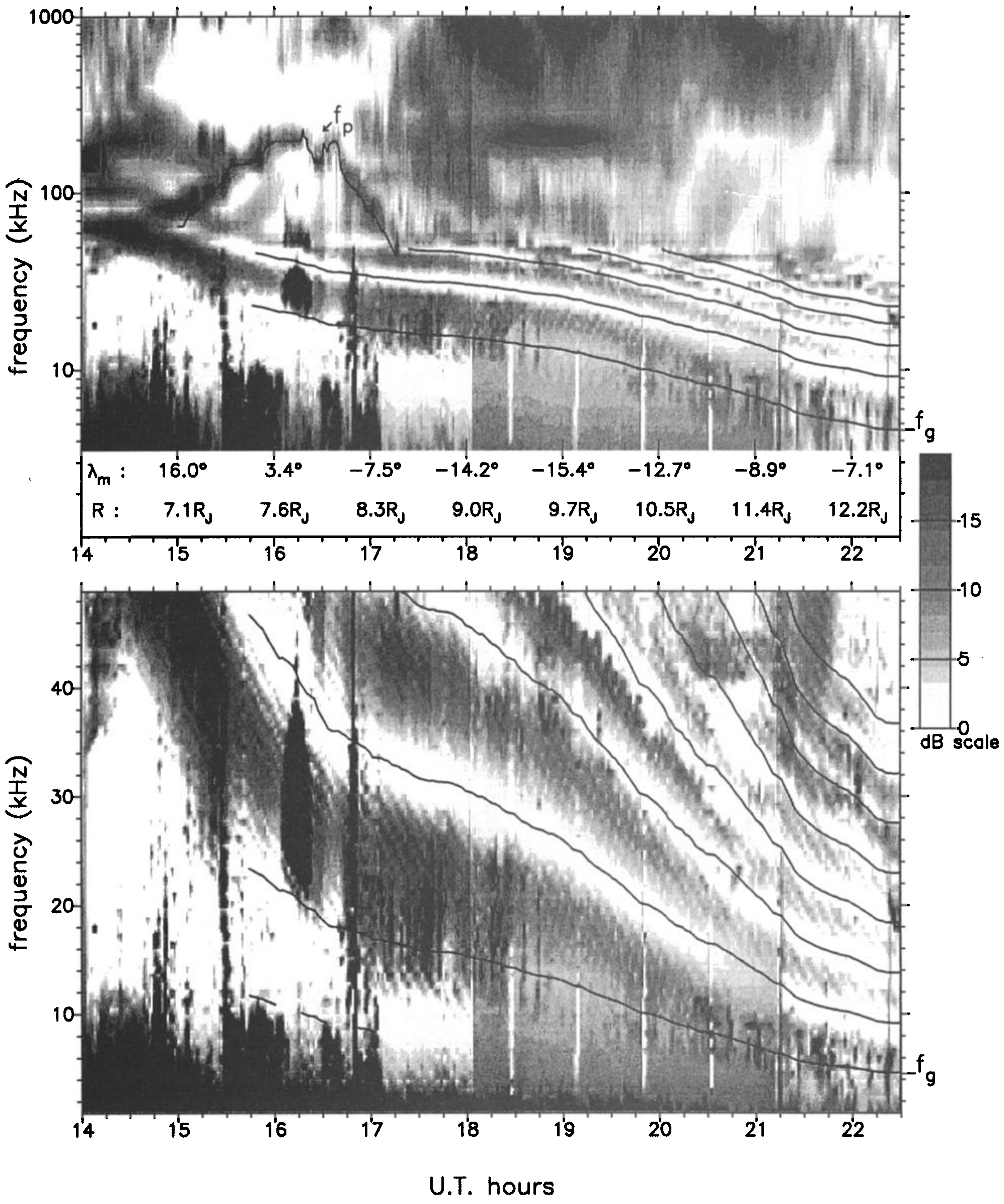

Fig. 1. Unified radio and plasma wave dynamic spectrum during encounter displayed as frequency versus time, with relative intensity indicated by the bar chart on the right. The torus traversal took place near 1400–1800 UT. We have superimposed in continuous lines the plasma frequency f_p deduced from the upper hybrid noise and harmonics of the electron gyrofrequency f_g (calculated from the data as explained in section 4.3). The distance to Jupiter R (in Jovian radii) and magnetic latitude λ_m are given in the middle panel. The dashed line near 1600 UT in the lower panel shows $f_g/2$ (see text).

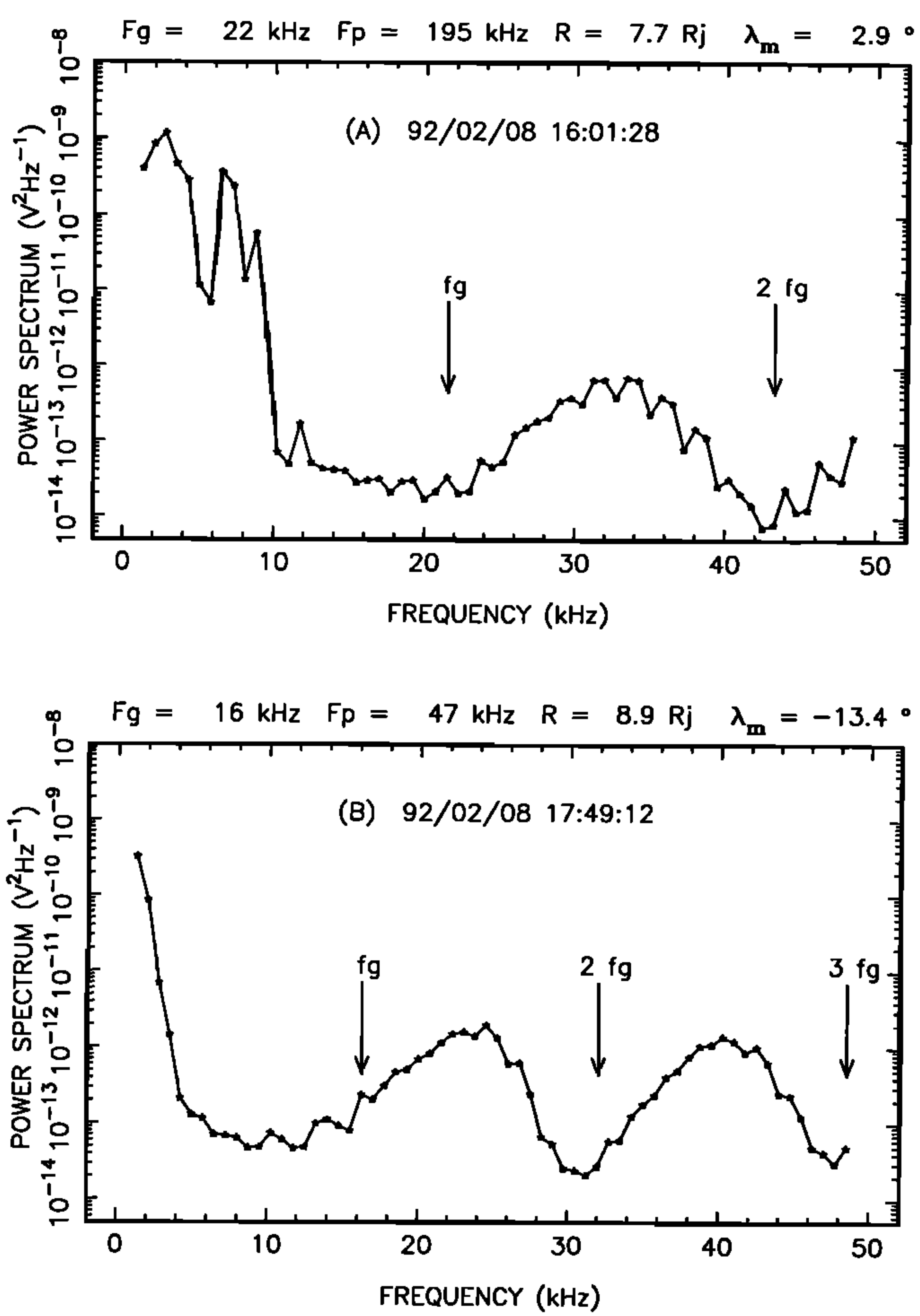

Fig. 2. Typical spectra in (*a*) the torus and (*b*) its outer fringe. The arrows indicate harmonics of the electron gyrofrequency f_g. The labels correspond to radial distance to Jupiter (R), magnetic latitude (λ_m), and plasma frequency (f_p).

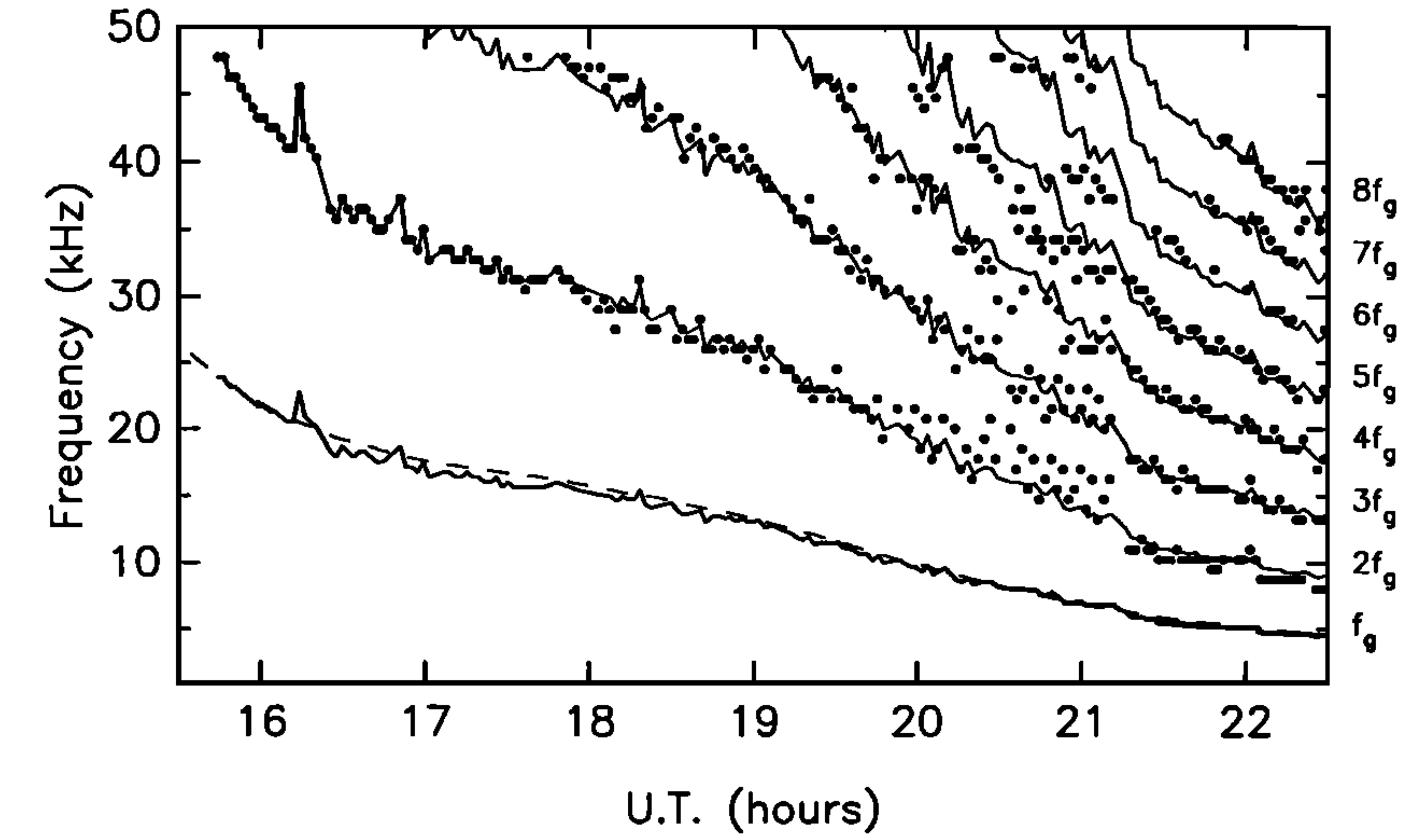

Fig. 9. Measured frequencies of the minima of the spectral shape (dots), together with the gyrofrequency and its harmonics computed by averaging the gyrofrequencies deduced from these minima (continuous lines). The gyrofrequency calculated from the magnetometer data (64-s averages; courtesy of A. Balogh) is shown for comparison as a dashed line.

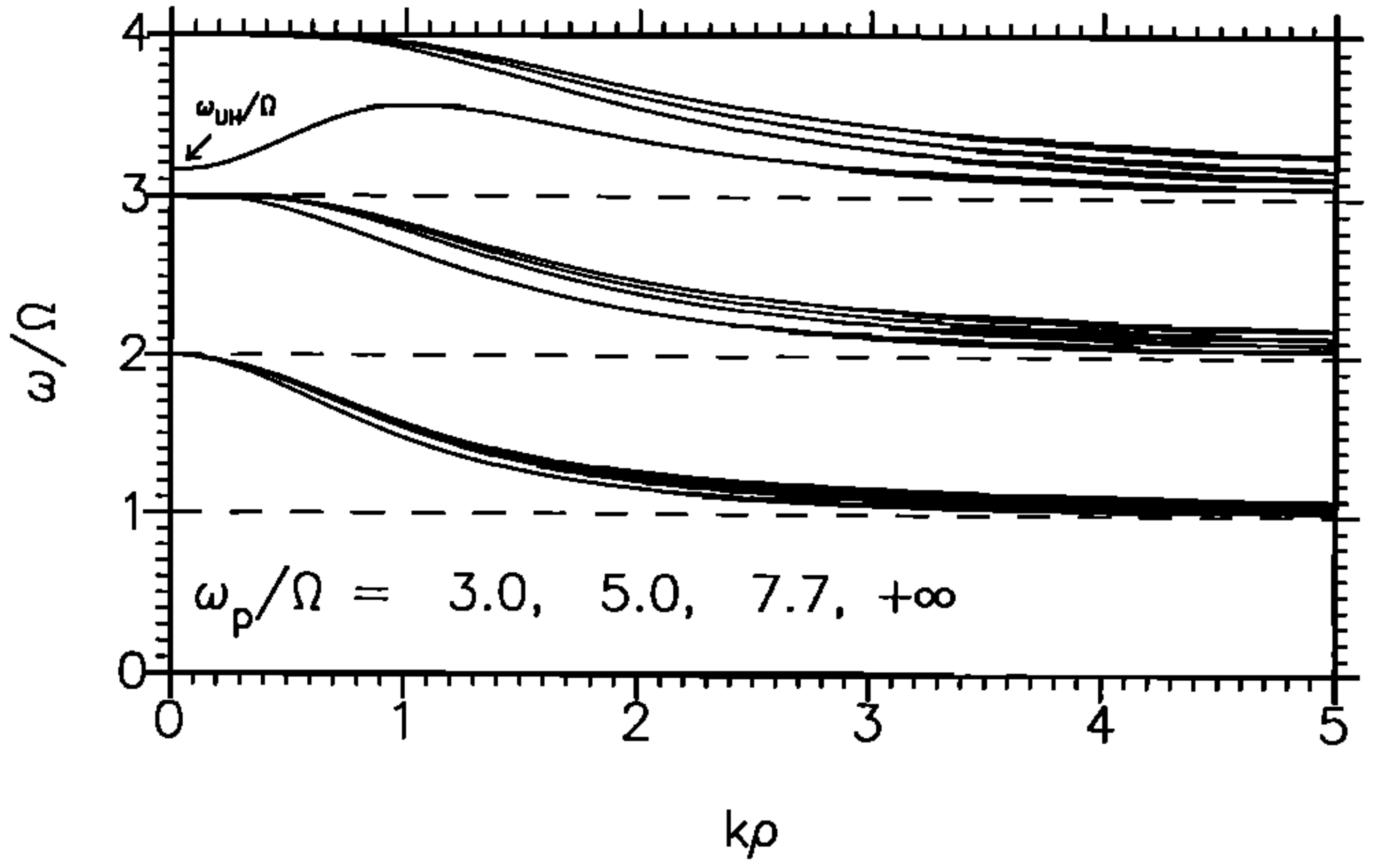

Fig. 5. Bernstein modes ($k = k_\perp$) drawn as ω/Ω versus $k\rho$ for different values of the parameter ω_p/Ω increasing from left to right. (The case $\omega_p/\Omega = 7.7$ corresponds to the spectrum of Figure 3*a*, and its first harmonic band is nearly identical to the limiting curve $\omega_p/\Omega \to \infty$ shown here for comparison.) The results correspond to a Maxwellian plasma but are not significantly changed by a very small proportion of suprathermal electrons.

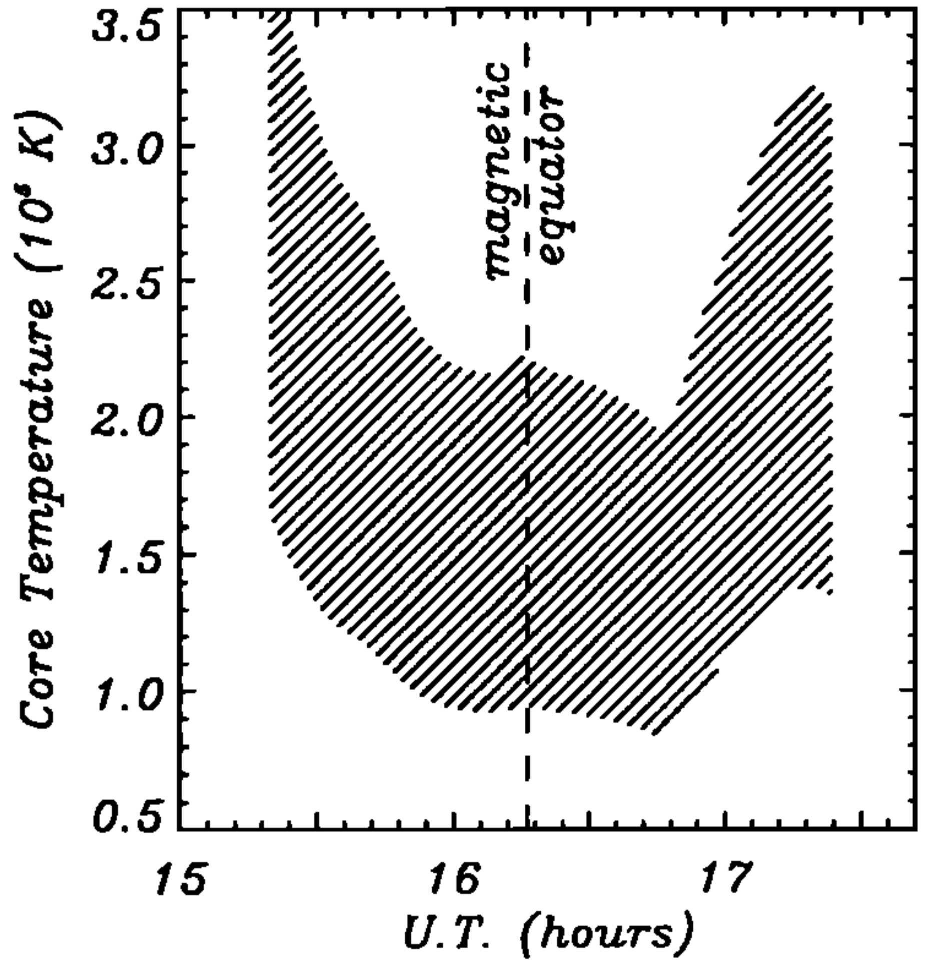

Fig. 8. Temperature (15 min averaged) as a function of time, deduced from the spin modulation of Bernstein waves from ~+11° to −11° magnetic latitude along Ulysses trajectory in the torus (at ~8 R_J from Jupiter). The shaded region sketches the maximum error bars, whose present large values are due to the very simple method used here.

10

Waves in a Hot Magnetized Plasma

$$\mathbf{v} \times \mathbf{B}_0 \cdot \boldsymbol{\nabla}_{\mathbf{v}} f_{s0} = 0 \tag{10.1.2}$$

$$\frac{\partial f_s}{\partial t} + \mathbf{v} \cdot \boldsymbol{\nabla} f_s + \frac{e_s}{m_s}(\mathbf{v} \times \mathbf{B}_0) \cdot \boldsymbol{\nabla}_{\mathbf{v}} f_s + \frac{e_s}{m_s}[\mathbf{E} + \mathbf{v} \times \mathbf{B}] \cdot \boldsymbol{\nabla}_{\mathbf{v}} f_{s0} = 0, \tag{10.1.3}$$

"Cylindrical Velocity-Space Coordinates"

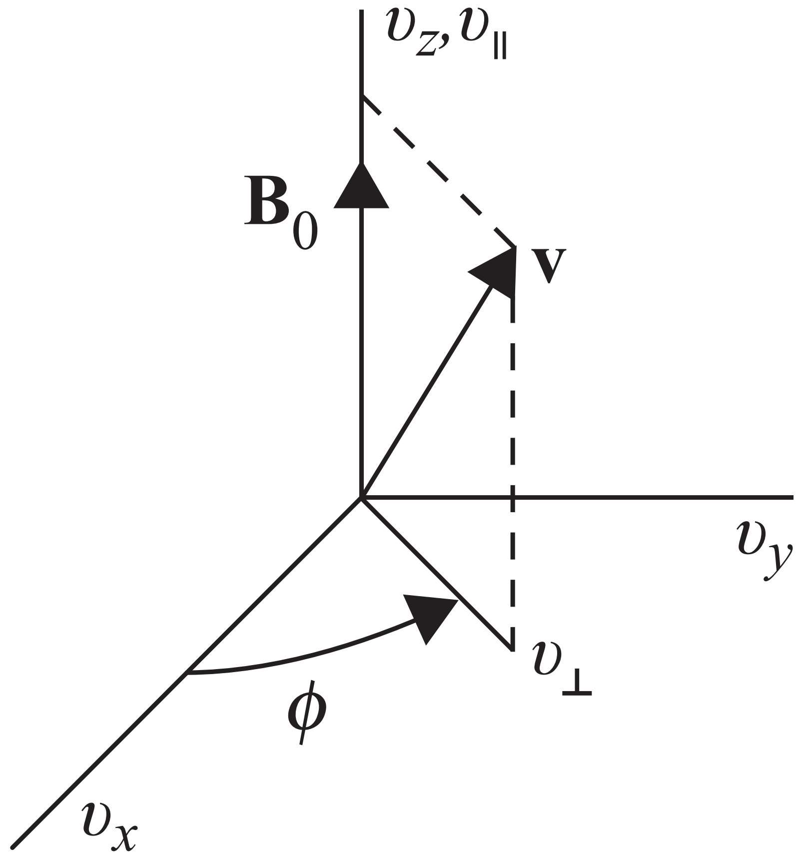

Figure 10.1 Cylindrical velocity space coordinates $v_\perp, v_\parallel$, and ϕ.

$$(-i\omega + i\mathbf{k}\cdot\mathbf{v})\tilde{f}_s - \omega_{cs}\frac{\partial \tilde{f}_s}{\partial \phi} + \frac{e_s}{m_s}[\tilde{\mathbf{E}} + \mathbf{v}\times\tilde{\mathbf{B}}]\cdot\nabla_{\mathbf{v}} f_{s0} = 0. \tag{10.1.10}$$

$$\mathbf{k}\cdot\mathbf{v} = k_\parallel v_\parallel + k_\perp v_\perp \cos\phi. \tag{10.1.12}$$

"Cylindrical Velocity-Space Coordinates"

$$\frac{\partial \tilde{f}_s}{\partial \phi} - \mathrm{i}(\alpha_s + \beta_s \cos\phi)\tilde{f}_s = \frac{e}{m_s \omega_{cs}}\left[\tilde{\mathbf{E}} + \mathbf{v} \times \overset{\tilde{\mathbf{B}}}{\left(\frac{\mathbf{k} \times \tilde{\mathbf{E}}}{\omega}\right)}\right] \cdot \nabla_{\mathbf{v}} f_{s0}, \tag{10.1.13}$$

$$\alpha_s = \frac{k_{\|} v_{\|} - \omega}{\omega_{cs}} \quad \text{and} \quad \beta_s = \frac{k_{\perp} v_{\perp}}{\omega_{cs}}. \tag{10.1.14}$$

10.2.1 The Harris Dispersion Relation

$$\tilde{\mathbf{E}} = -i\mathbf{k}\tilde{\Phi} \quad \tilde{\mathbf{B}} = \mathbf{k} \times \tilde{\mathbf{E}} = 0$$

$$\frac{\partial \boxed{\tilde{f}_s}}{\partial \phi} - \mathrm{i}(\alpha_s + \beta_s \cos\phi)\boxed{\tilde{f}_s} = \frac{-\mathrm{i}e_s}{m_s \omega_{cs}} \tilde{\Phi}\mathbf{k} \cdot \boldsymbol{\nabla}_{\mathbf{v}} f_{s0}. \tag{10.2.1}$$

$$\frac{\mathrm{d}f}{\mathrm{d}x} + P(x)f = Q(x), \tag{10.2.2}$$

$$k^2\tilde{\Phi} = \sum_s \frac{e_s}{\epsilon_0} \int_{-\infty}^{\infty} \boxed{\tilde{f}_s} \mathrm{d}^3 v. \tag{10.2.7}$$

Jacobi-Anger Expansion

$$\tilde{E}_0 e^{i(k_\perp x - \omega t)} = \tilde{E}_0 e^{i\beta \sin \omega_c t}\, e^{-i\omega t} = \tilde{E}_0 \sum_{n=-\infty}^{\infty} J_n(\beta) e^{in\omega_c t}\, e^{-i\omega t}$$

$$x = \rho_c \sin \omega_c t,$$

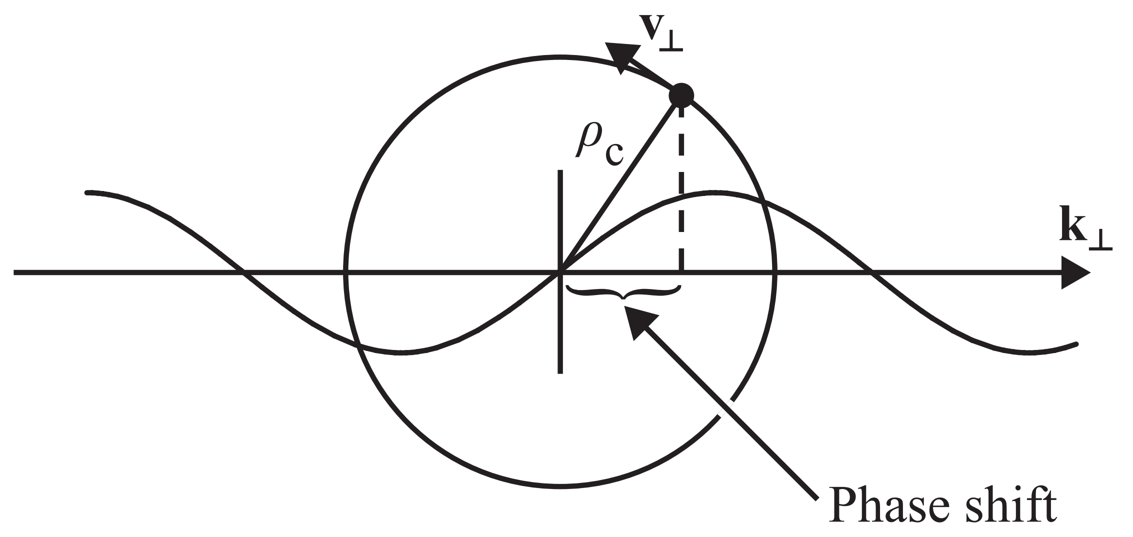

$$\beta \equiv k_\perp \rho$$

Figure 10.3 For a finite cyclotron radius, ρ_c, a phase shift is introduced by the cyclotron motion of the particle around the magnetic field. This phase shift is responsible for the resonances at $n\omega_c$.

$$\beta_s = k_\perp v_\perp / \omega_{cs}$$

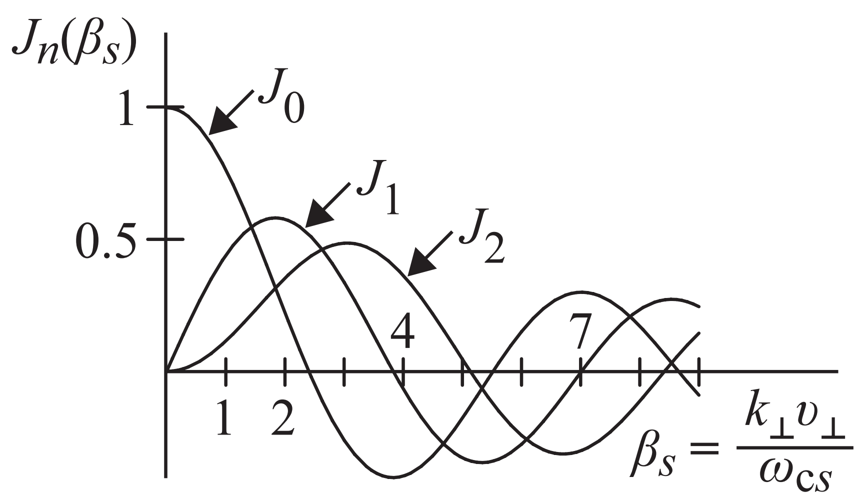

Figure 10.4 Plots of the zero-order, first-order, and second-order Bessel functions, $J_0(\beta_s)$, $J_1(\beta_s)$, and $J_2(\beta_s)$.

$$\tilde{f}_s = \frac{-\mathrm{i} e_s n_s \tilde{\Phi}}{m_s \omega_{\mathrm{c}s}} \, \mathrm{e}^{\mathrm{i}(\alpha_s \phi + \beta_s \sin\phi)} \int^{\phi} \mathbf{k} \cdot \boldsymbol{\nabla}_{\mathbf{v}} F_{s0} \, \mathrm{e}^{-\mathrm{i}(\alpha_s \phi' + \beta_s \sin\phi')} \mathrm{d}\phi', \qquad (10.2.5)$$

$$\begin{aligned} Đ(k,\omega) = 1 + \sum_s \frac{\omega_{\mathrm{p}s}^2}{k^2 \omega_{\mathrm{c}s}} \int \mathrm{e}^{\mathrm{i}(\alpha_s \phi + \beta_s \sin\phi)} \\ \times \int^{\phi} \mathrm{i}\mathbf{k} \cdot \boldsymbol{\nabla}_{\mathbf{v}} F_{s0} \, \mathrm{e}^{-\mathrm{i}(\alpha_s \phi' + \beta_s \sin\phi')} \mathrm{d}\phi' \, \mathrm{d}\phi \upsilon_\perp \, \mathrm{d}\upsilon_\perp \, \mathrm{d}\upsilon_\parallel = 0, \qquad (10.2.8) \end{aligned}$$

$$e^{-i\beta_s \sin\phi'} = \sum_{n=-\infty}^{\infty} J_n(\beta_s)\, e^{-in\phi'}, \tag{10.2.11}$$

$$\begin{aligned}\int^{\phi} e^{-i(\alpha_s\phi' + \beta_s \sin\phi')}\, d\phi' &= \sum_n J_n(\beta_s) \int^{\phi} e^{-i(\alpha_s + n)\phi'}\, d\phi' \\ &= i\sum_n \frac{J_n(\beta_s)}{\alpha_s + n}\, e^{-i(\alpha_s + n)\phi}.\end{aligned} \tag{10.2.12}$$

$$\begin{aligned}&\int^{\phi} (e^{i\phi'} + e^{-i\phi'})\, e^{-i(\alpha_s\phi' + \beta_s \sin\phi')}\, d\phi' \\ &= \sum_n J_n(\beta_s) \int^{\phi} [e^{-i(\alpha_s - 1 + n)\phi'} + e^{-i(\alpha_s + 1 + n)\phi'}]\, d\phi' \\ &= i\sum_n J_n(\beta_s) \left[\frac{e^{-i(\alpha_s - 1 + n)\phi}}{\alpha_s - 1 + n} + \frac{e^{-i(\alpha_s + 1 + n)\phi}}{\alpha_s + 1 + n}\right].\end{aligned} \tag{10.2.13}$$

gives

$$e^{i(\alpha_s\phi+\beta_s\sin\phi)}\int^{\phi}\cdots d\phi' = -k_{\parallel}\frac{\partial F_{s0}}{\partial \upsilon_{\parallel}}\sum_{n,m} J_m J_n\left[\frac{e^{i(m-n)\phi}}{\alpha_s+n}\right]$$
$$-\frac{1}{2}k_{\perp}\frac{\partial F_{s0}}{\partial \upsilon_{\perp}}\sum_{n,m} J_m J_n\left[\frac{e^{i(m-n+1)\phi}}{\alpha_s+n-1}+\frac{e^{i(m-n-1)\phi}}{\alpha_s+n+1}\right]. \tag{10.2.15}$$

In the second summation, the index can be relabeled to give

$$\sum_{n,m}\frac{J_m J_{n+1}}{\alpha_s+n}e^{i(m-n)\phi}+\frac{J_m J_{n-1}}{\alpha_s+n}e^{i(m-n)\phi} = \sum_{n,m} J_m[J_{n+1}+J_{n-1}]\frac{e^{i(m-n)\phi}}{\alpha_s+n}. \tag{10.2.16}$$

Using the Bessel function recursion formula, $J_{n+1}+J_{n-1}=(2n/\beta_s)J_n$, this sum can be written in the more compact form

$$\sum_{m,n}\frac{2n\, J_m J_n}{\beta_s(\alpha_s+n)}e^{i(m-n)\phi}. \tag{10.2.17}$$

$$
\begin{aligned}
Đ(k,\omega) = 1 - \sum_s \frac{\omega_{\mathrm{p}s}^2}{k^2\omega_{\mathrm{c}s}} \sum_{n,m} \int_{-\infty}^{\infty} \int_0^{\infty} \upsilon_\perp \mathrm{d}\upsilon_\perp \, \mathrm{d}\upsilon_\parallel \frac{J_m J_n}{\alpha_s + n} \\
\times \left[k_\parallel \frac{\partial F_{s0}}{\partial \upsilon_\parallel} + \frac{n\,\omega_{\mathrm{c}s}}{\upsilon_\perp} \frac{\partial F_{s0}}{\partial \upsilon_\perp} \right] \int_0^{2\pi} \mathrm{e}^{\mathrm{i}(m-n)\phi} \, \mathrm{d}\phi = 0.
\end{aligned}
\qquad (10.2.19)
$$

$$\mathcal{D}(k,\omega) = 1 - \sum_s \frac{\omega_{ps}^2}{k^2} \sum_n \int_{-\infty}^{\infty} \int_0^{\infty} \frac{J_n^2(k_\perp \upsilon_\perp/\omega_{cs})}{k_\parallel \upsilon_\parallel - \omega + n\omega_{cs}} \left[k_\parallel \frac{\partial F_{s0}}{\partial \upsilon_\parallel} + \frac{n\omega_{cs}}{\upsilon_\perp} \frac{\partial F_{s0}}{\partial \upsilon_\perp} \right]$$

$$\times 2\pi \upsilon_\perp \mathrm{d}\upsilon_\perp \mathrm{d}\upsilon_\parallel = 0. \tag{10.2.20}$$

This equation is called the Harris dispersion relation after Harris (1959), who first derived this result.

10.2.2 The Low-temperature, Long-Wavelength Limit

$$Đ(k,\omega) = 1 - \sum_s \frac{\omega_{ps}^2}{k^2} \sum_n \int_{-\infty}^{\infty} \int_0^{\infty} \frac{J_n^2(k_\perp \upsilon_\perp/\omega_{cs})}{k_\| \upsilon_\| - \omega + n\omega_{cs}} \left[k_\| \frac{\partial F_{s0}}{\partial \upsilon_\|} + \frac{n\omega_{cs}}{\upsilon_\perp} \frac{\partial F_{s0}}{\partial \upsilon_\perp} \right]$$

$$\times 2\pi \upsilon_\perp \mathrm{d}\upsilon_\perp \mathrm{d}\upsilon_\| = 0. \qquad (10.2.20)$$

$$Đ_0(k,\omega) = \left[1 - \sum_s \frac{\omega_{ps}^2}{\omega^2}\right] \cos^2\theta + \left[1 - \sum_s \frac{\omega_{ps}^2}{\omega^2 - \omega_{cs}^2}\right] \sin^2\theta = 0, \qquad (10.2.22)$$

10.2.3 The Bernstein Modes

$$Đ(k_\perp, \omega) = 1 - \frac{\omega_p^2}{k_\perp^2} \sum_{n=-\infty}^{\infty} \frac{n\omega_c}{-\omega + n\omega_c} \times \int_{-\infty}^{\infty} \int_0^{\infty} J_n^2\left(\frac{k_\perp \upsilon_\perp}{\omega_c}\right) \frac{\partial F_0}{\partial \upsilon_\perp} 2\pi \mathrm{d}\upsilon_\perp \mathrm{d}\upsilon_\parallel = 0, \tag{10.2.24}$$

$$\frac{n\omega_c}{-\omega + n\omega_c} + \frac{(-n)\omega_c}{-\omega + (-n)\omega_c} = \frac{-2n^2\omega_c^2}{\omega^2 - n^2\omega_c^2}, \tag{10.2.25}$$

$$Đ(k_\perp, \omega) = 1 + \frac{2\omega_p^2}{k_\perp^2} \sum_{n=1}^{\infty} \frac{n^2\omega_c^2}{\omega^2 - n^2\omega_c^2} \times \int_{-\infty}^{\infty} \int_0^{\infty} J_n^2\left(\frac{k_\perp \upsilon_\perp}{\omega_c}\right) \frac{\partial F_0}{\partial \upsilon_\perp} 2\pi \mathrm{d}\upsilon_\perp \mathrm{d}\upsilon_\parallel = 0, \tag{10.2.26}$$

10.2.3 The Bernstein Modes

$$Đ(k_\perp, \omega) = 1 - \sum_{n=1}^{\infty} \frac{2\omega_p^2}{\beta_c^2 \omega_c^2} \frac{\Gamma_n(\beta_c)}{(\omega/n\,\omega_c)^2 - 1} = 0, \tag{10.2.29}$$

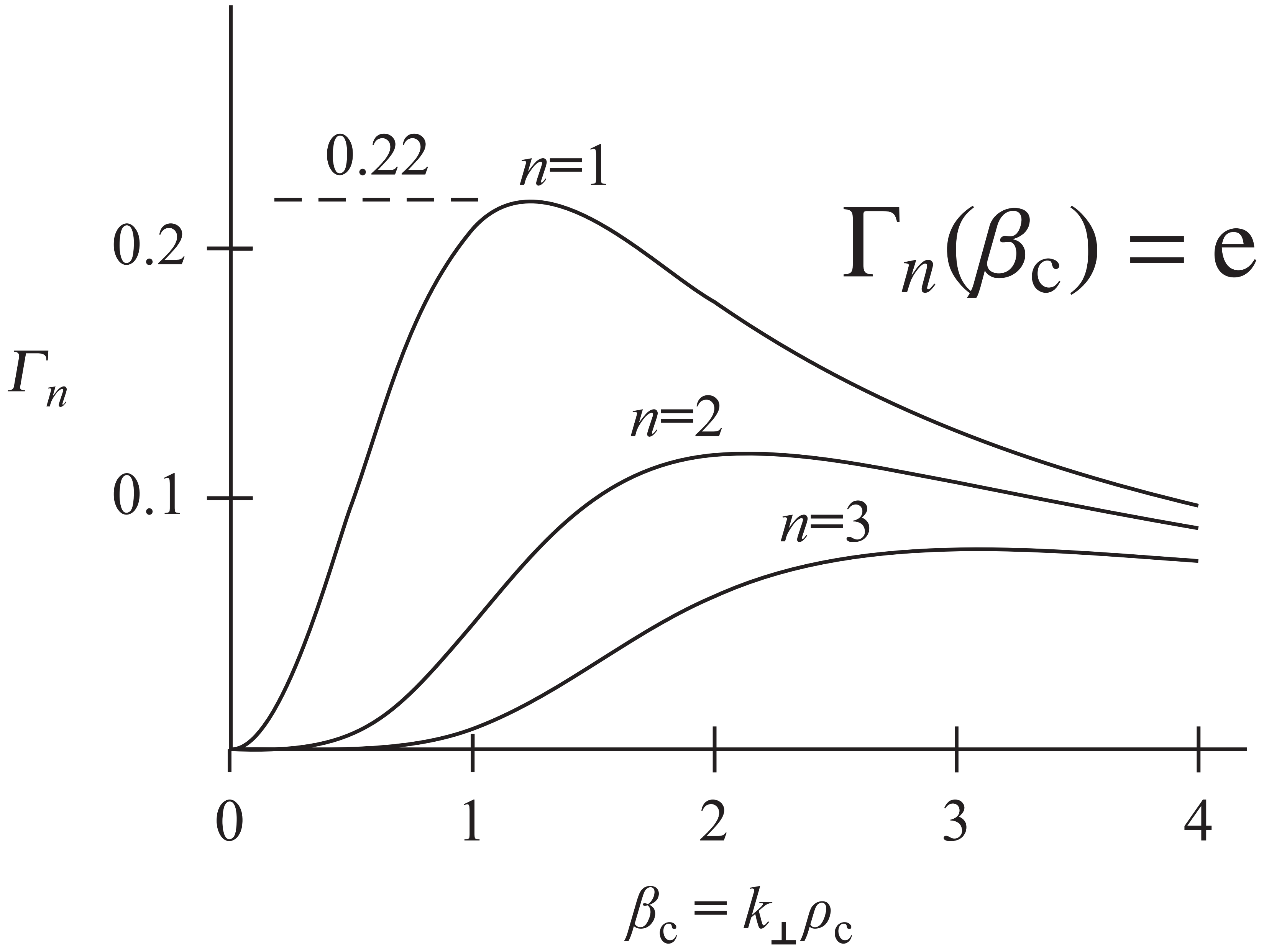

$$\Gamma_n(\beta_c) = e^{-\beta_c^2} I_n(\beta_c^2), \tag{10.2.30}$$

Figure 10.6 Plots of $\Gamma_n(\beta_c)$ for n = 1, 2, and 3.

10.2.3 The Bernstein Modes

$$Đ(k_\perp, \omega) = 1 - \sum_{n=1}^{\infty} \frac{2\omega_p^2}{\beta_c^2 \omega_c^2} \frac{\Gamma_n(\beta_c)}{(\omega/n\,\omega_c)^2 - 1} = 0, \tag{10.2.29}$$

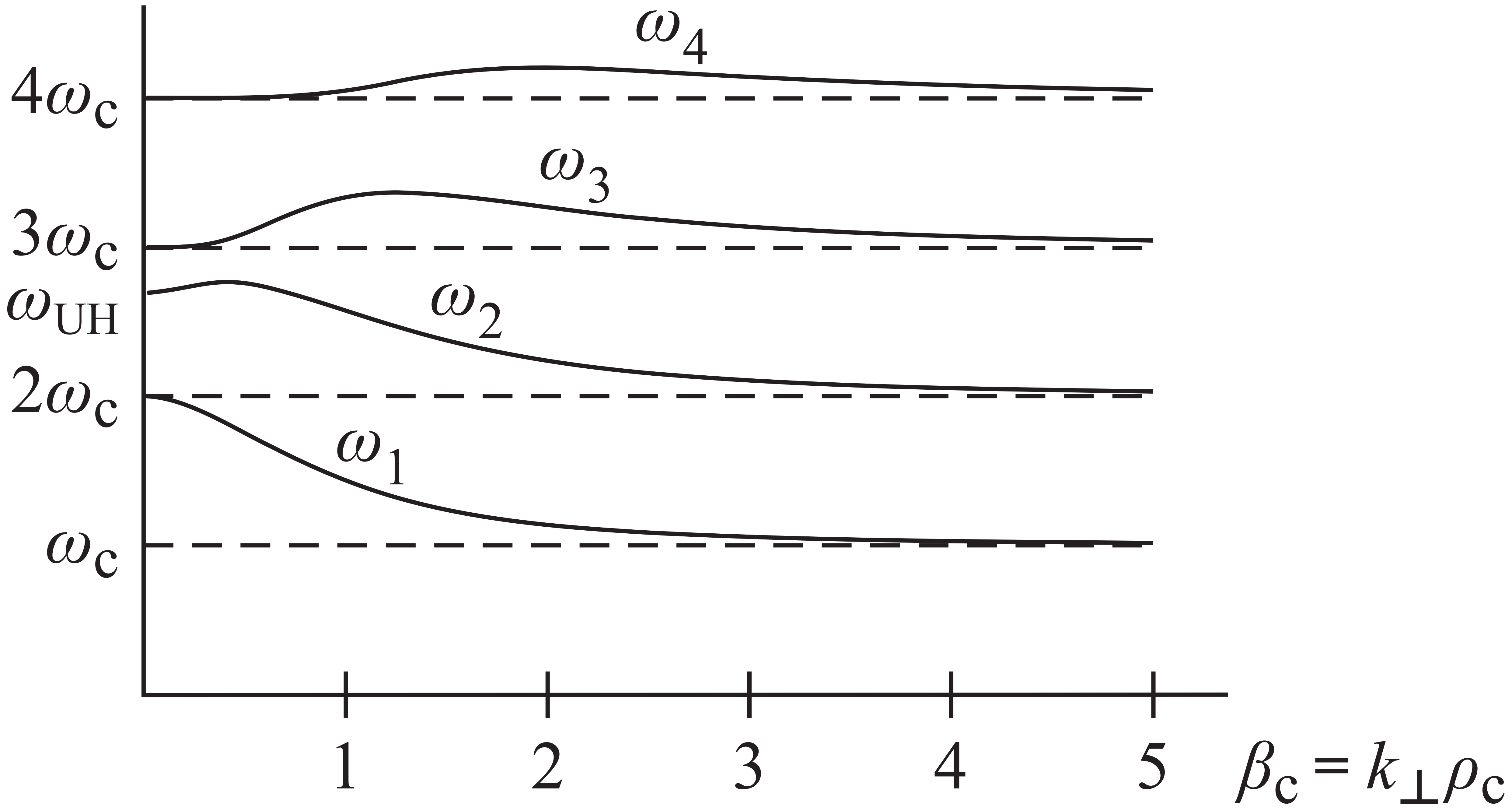

Figure 10.8 A plot of the solutions of $Đ(k_\perp, \omega) = 0$ as a function of the perpendicular wave number, $k_\perp$. These solutions are called the Bernstein modes.

Next Lecture…

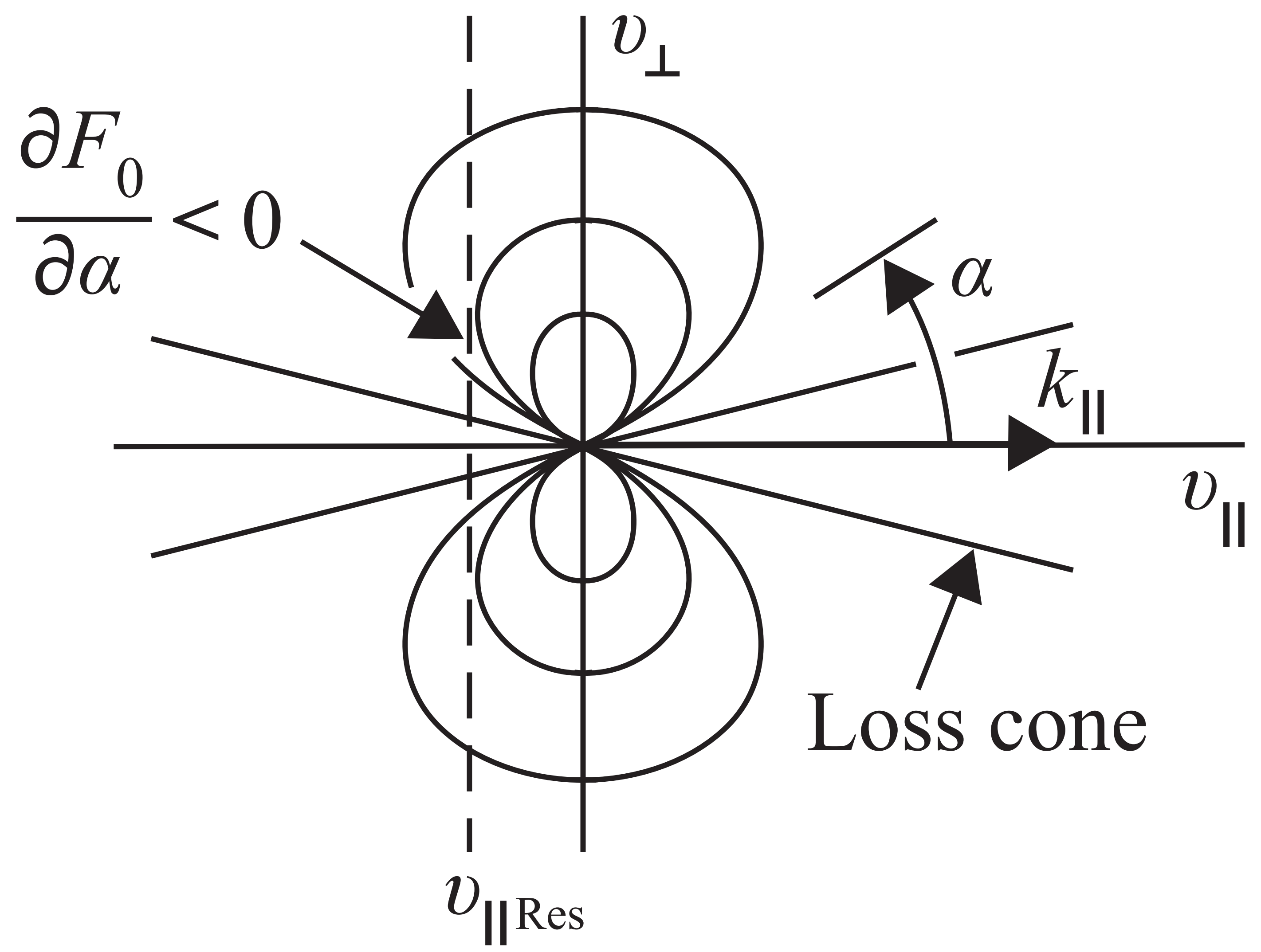

Figure 10.25 A loss-cone electron velocity distribution showing the cyclotron resonance velocity, $v_{\parallel\text{Res}}$, for a whistler-mode wave propagating in the $k_\parallel$ direction.